Fast, robust and laser-free universal entangling gates for trapped-ion quantum computing

Markus Nünnerich,[1] Daniel Cohen,[2] Patrick Barthel,[1] Patrick H. Huber,[1] Dorna Niroomand,[1] Alex Retzker,[2,3] and Christof Wunderlich[1]

[1] *Department of Physics, School of Science and Technology, University of Siegen, 57068 Siegen, Germany*
[2] *Racah Institute of Physics, Hebrew University of Jerusalem, 91904 Jerusalem, Israel*
[3] *AWS Center for Quantum Computing, Pasadena, CA 91125, USA*

(Dated: March 18, 2024)

A novel two-qubit entangling gate for RF-controlled trapped-ion quantum processors is proposed theoretically and demonstrated experimentally. The speed of this gate is an order of magnitude higher than that of previously demonstrated two-qubit entangling gates in static magnetic field gradients. At the same time, the phase-modulated field driving the gate, dynamically decouples the qubits from amplitude and frequency noise, increasing the qubits' coherence time by two orders of magnitude. The gate requires only a single continuous RF field per qubit, making it well suited for scaling a quantum processor to large numbers of qubits. Implementing this entangling gate, we generate the Bell states $|\Phi^+\rangle$ and $|\Psi^+\rangle$ in ≤ 313 μs with fidelities up to 98^{+2}_{-3} % in a static magnetic gradient of only 19.09 T/m. At higher magnetic field gradients, the entangling gate speed can be further improved to match that of laser-based counterparts.

I. INTRODUCTION

Trapped atomic ions are a physical platform well suited for quantum information processing [1, 2]. Intense research into this platform has lead to outstanding performance of trapped-ion quantum processors using laser-controlled ionic qubits [3–6].

Trapped ions controlled by radio frequency (RF) signals are particularly suited for scaling up quantum computers, since technological challenges associated with using laser light for coherent control of qubits are avoided in this laser-free approach [7–11]. With RF-controlled ions high fidelity single- and two-qubit gates have been achieved [12–16], as well as low cross-talk suitable for fault-tolerant quantum computing [17]. Also, complete quantum algorithms were implemented using RF-controlled ions [18, 19]. So far, however, two-qubit gate speed has lagged behind its laser-based counterparts [15]. Here, we introduce and experimentally realize a novel two-qubit entangling gate with gate speed an order of magnitude faster than previous RF-gates in static magnetic field gradients. Another feature of this gate is its built-in robustness against external noise making additional dynamical decoupling superfluous. Furthermore, only a single modulated RF-driving field per ion is required for its operation, further simplifying the scaling up of trapped-ion quantum computers.

II. EXPERIMENTAL OVERVIEW

We investigate double dressed state dynamics of a single qubit and implement conditional quantum dynamics with two qubits using $^{171}Yb^+$ ions trapped in a macroscopic linear Paul trap with radial and axial trapping frequencies of $2\pi \times 380$ kHz and $\nu = 2\pi \times 98.08$ kHz, respectively. The experimental setup is similar to [16] and only briefly described here. The two qubits are encoded in hyperfine states of the electronic ground state of $^{171}Yb^+$ ions, $|0\rangle \equiv |^2S_{1/2}, F = 0, m_F = 0\rangle$ and $|1\rangle \equiv |^2S_{1/2}, F = 1, m_F = -1\rangle$. A static magnetic field gradient of 19.09(1) T/m applied along the trap axis (z-axis) yields individual Zeeman-shifts of the two qubits and results in individual resonance frequencies near $2\pi \times 12.6$ GHz, $\omega_0^{(1)}$ and $\omega_0^{(2)}$, of the magnetic dipole transition between qubit states. Thus, qubits are individually coherently controlled with low cross-talk using global RF radiation near $2\pi \times 12.6$ GHz [17]. The entangling gate proposed and implemented here takes advantage of a state selective force induced by the static magnetic gradient field coupling the internal qubit states to the axial vibrational states of the 2-ion crystal [7]. Therefore, when using magnetic gradient induced coupling (MAGIC), laser light is not required for implementing conditional gates with trapped ions.

The ions are cooled close to their motional ground state in two stages. Initial Doppler cooling is followed by RF sideband cooling of both present vibrational modes giving a mean phonon number of 0.6(5) in the center-of-mass (COM) mode measured with sideband thermometry [20]. The heating rate of one trapped ion in the current experimental setup is 0.19(3) phonons/ms for this mode.

We use an Arbitrary Waveform Generator (AWG) to generate the phase-modulated RF driving field that double dresses both qubits, as in[21–23]. The driving field's action on the qubits is described by the Hamiltonian

$$H_D = \sum_{j=1,2} \Omega_1^{(j,\mathrm{Amp})} \sigma_x^{(j)} \times \cos\left(\omega_0^{(j)} t + \frac{\Omega_2}{\Omega_1^{(j,\mathrm{Phase})}} \sin\left(\Omega_1^{(j,\mathrm{Phase})} t\right)\right) \quad (1)$$

where $\omega_0^{(j)}$ is the j-th qubit's transition frequency, σ_x is a Pauli matrix, and Ω_2 is a parameter quantifying the

phase modulation amplitude. For this article we set $\hbar = 1$ while all occurring frequencies are angular frequencies. $\Omega_1^{(j,\mathrm{Amp})}$ is the Rabi frequency determined by the RF field amplitude for qubit j and $\Omega_1^{(j,\mathrm{Phase})}$ is set as a parameter to create the second dressing field for the qubits via phase modulation. For our gate scheme, we choose $\Omega_1^{\mathrm{Amp}} = \Omega_1^{\mathrm{Phase}}$, (optimization over this condition may result in longer coherence time [24]). To ensure $\Omega_1^{\mathrm{Amp}} = \Omega_1^{\mathrm{Phase}}$, a calibration of RF-amplitudes is carried out by recording and fitting Rabi oscillations of each individual qubit. The effect on the entangling gate in case of detuned Rabi frequencies is investigated in appendix F.

First, in Sec. III, we focus on the effect of the double dressing field according to Eq. (1) on individual qubits. Then, we describe the experimental procedure and results for the entangling gate in Sec. IV.

III. DOUBLE DRESSING OF SINGLE QUBITS

The MAGIC scheme requires a magnetic sensitive qubit transition, making the qubits therefore susceptible to decoherence due to magnetic field fluctuations. We demonstrate experimentally that the double dressing field acts as continuous dynamical decoupling and improves the coherence time significantly, by suppressing the effect of addressing frequency fluctuations as well as amplitude fluctuations of the RF driving field. The idea of using double dressed states to counter noise has been established in previous works on nitrogen-vacancy centers in diamond [23–25]. Here, we extend double dressing to individual trapped ions, and investigate the coupling of the qubit resonance to vibrational modes by the phase modulated driving field.

The double dressed scheme is illustrated for one qubit in Fig. 1 and is described in appendix A in detail. In brief, the ionic qubit in a harmonic oscillator potential is modeled as

$$H = \frac{\omega_0}{2}\sigma_z + \nu b^\dagger b + \frac{\eta\nu}{2}\sigma_z\left(b + b^\dagger\right). \tag{2}$$

Here, we include the COM vibrational mode and denote b as the ladder operator of the motional quanta in the effective harmonic trapping potential. ν is the motional mode frequency and $\eta = g_I\mu_B(\partial_z B)\nu^{-3/2}/\sqrt{2Nm_{\mathrm{Yb}}}$ is the effective Lamb-Dicke parameter proportional to the magnetic field gradient $(\partial_z B)$ [7]. g_I is the effective g-factor in the electronic ground state of $^{171}\mathrm{Yb}^+$, m_{Yb} is the mass of ^{171}Yb, μ_B is Bohr's magneton, and N is the number of ions in a linear Coulomb crystal. When turning on the driving field (Eq. (1)), we obtain the Hamiltonian,

$$H_I = \frac{\Omega_1}{2}S_z + \frac{\Omega_2}{2}S_x\cos(\Omega_1 t) + \nu b^\dagger b - \frac{\eta\nu}{2}S_x\left(b + b^\dagger\right), \tag{3}$$

in the rotating frame *w.r.t.* $\omega_0/2\sigma_z$. Here, $S_x = \sigma_z, S_y = \sigma_y, S_z = -\sigma_x$ are the dressed basis operators. Dressing suppresses fluctuations of the bare state energy gap

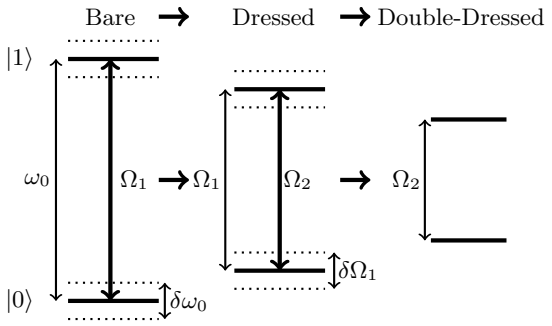

Figure 1: Illustration of the emergence of double-dressed states and the consequent protection against frequency and amplitude fluctuations. Thin double arrows indicate resonance frequencies. Thick double arrows indicate Rabi frequencies. The bare qubit is driven near resonance, ω_0 with a time dependent detuning achieved by phase modulation according to Eq. (1) (left: Bare). In the dressed state basis (middle: Dressed), the drive with Rabi frequency Ω_1 translates into the energy gap Ω_1. Relative frequency fluctuations $\delta\omega_0$ between driving field and qubit are suppressed in the dressed basis for $\delta\omega_0 \ll \Omega_1$. The phase modulation transforms into an effective on-resonance drive in the dressed basis, creating double dressed states (right: Double-Dressed). In the double-dressed frame, the effective second drive translates into the double-dressed states energy gap. Amplitude fluctuations in the first drive $\delta\Omega_1$ are suppressed in the double-dressed basis for $\delta\Omega_1 \ll \Omega_2$.

$\delta\omega_0 \ll \Omega_1$ caused by either frequency fluctuations of the driving field, or by fluctuations of magnetically sensitive bare qubit states. Phase modulation of the dressing field, in addition, suppresses fluctuations in the amplitude of Ω_1: Phase modulation creates, in an appropriate rotating frame, an effective on-resonance second drive in the dressed basis. This second drive dresses the qubit a second time, and thus dynamically decouples amplitude noise fluctuations in the drive $\delta\Omega_1$, which would otherwise reduce the coherence time of the dressed qubit. These fluctuations are suppressed as long as $\delta\Omega_1 \ll \Omega_2$. Furthermore, undesired coupling of the qubit to the motional state, which leads to a decay in the Rabi oscillations, is suppressed as long as $\Omega_2 \gg \eta\nu$ and $|\Omega_1 - \nu| \ll \Omega_2 \ll |\Omega_1 + \nu|$ (see appendix A for a detailed description).

A. Extending the coherence time

The impact of the phase modulated dressing field on a qubit's coherence time is shown in Fig. 2. We study the relaxation of a single qubit initialized in state $|0\rangle$, while the phase-modulated driving field given in Eq. (1) is continuously applied. Note, that this is an equal superposition state in the dressed basis, therefore, by fitting the decay of the oscillations' contrast to an exponential decay we can extract the coherence time $T_{2,\rho}$ of the dressed state. For $\Omega_2/\Omega_1 = 0.75$, used for the entangling gate mechanism, we observe two orders of magnitude improvement in $T_{2,\rho}$, up to 0.27(2) s. The reduced coher-

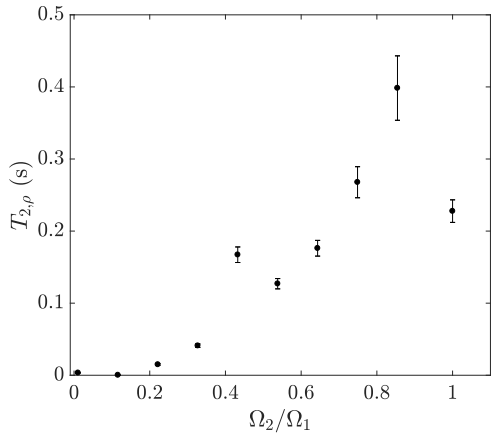

Figure 2: Relaxation time $T_{2,\rho}$ of a single qubit as a function of the modulation depth Ω_2/Ω_1. The qubit is initialized in state $|0\rangle$, which is a superposition state in the dressed state basis. The phase-modulated driving field is continuously applied and the coherence time $T_{2,\rho}$ is extracted from a exponential decay of the Rabi fringe contrast. At a modulation depth $\Omega_2/\Omega_1 \approx 0.75$, the relaxation time is enhanced by two orders of magnitude compared to the scenario without second dressing field.

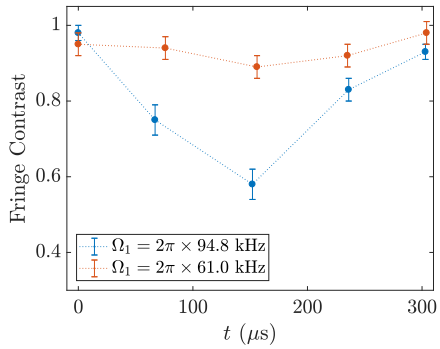

Figure 3: Entanglement and disentanglement of qubit states and motional states of a single ion by application of a phase modulated field (Eq.(1)) for the duration of a two-qubit gate. For Rabi frequency $\Omega_1 = 2\pi \times 94.8$kHz, close to the secular trap frequency, entanglement is signified by a maximal reduction of Ramsey fringe contrast at $t = 150\mu$s, which corresponds to approximately half the two-qubit gate time. At $t = 300\mu$s, qubit and motion are disentangled again, signified by a recovery of the fringe contrast. For Rabi frequency $\Omega_1 = 2\pi \times 61.0$kHz, qubit-phonon coupling, and, therefore, qubit-phonon entanglement is smaller, resulting in a smaller reduction of fringe contrast halfway through the gate. The dotted lines are added to guide the eye.

ence time for $\Omega_2/\Omega_1 \approx 1$ is either explained by second-order fluctuations of $\delta\Omega_2$ [23] or by the quantum stark shift induced by the counter rotating terms.

B. Coupling to the motional degrees-of-freedom

The interaction between the qubits' internal state is mediated via the ions' common vibrational motion. Therefore, we investigate the qubit-phonon coupling, first with a single ion. We do this by probing a qubit's coherence in a Ramsey-type experiment. An initial resonant $\pi/2$-pulse prepares the qubit in the eigenstate $|+\rangle$ of the driving field. Then the phase-modulated driving field is applied creating an initial spin-lock condition. A final $\pi/2$-pulse with variable phase projects the state vector into the $z-$basis, creating Ramsey fringes. Since the phase-modulated driving field is continuously applied, the state vector experiences continuous Rabi oscillations, traversing the Bloch sphere. Therefore, to map the coherence, we aim to apply the second Ramsey pulse while the state vector is in a coherent superposition on the Bloch sphere equator. We confirm the required evolution time by a projective measurement along the $z-$axis to ensure the Bloch vector being located in the equatorial plane of the Bloch sphere prior to Ramsey readout. Fig. 3 depicts the Ramsey fringe contrast measured as outlined above, for multiple steps in time up to the approximate entangling gate time of 300 μs, at $\Omega_1 = 2\pi\times$ 94.8 kHz and $\Omega_1 = 2\pi\times$ 61 kHz, respectively. In both cases, $\Omega_2/\Omega_1 = 0.75$. At $\Omega_1 = 2\pi\times$ 94.8 kHz, close to the axial trap frequency, significant qubit-phonon entanglement at about 150 μs occurs, indicated by the reduction of the qubit's internal coherence.

We see in Fig. 3 the recovery of the Ramsey fringe contrast after the full duration of the entangling gate's time ($\approx 300\mu$s). At this time, the ion's internal qubit states are disentangled again from the vibrational motion. This is the desired condition after an entangling gate has been completed, as described in Sec. IV. For comparison, at $\Omega_1 = 2\pi\times 61$ kHz where the ion-phonon coupling is weak, a smaller reduction of the fringe contrast in Fig. 3 occurs.

IV. TWO-QUBIT ENTANGLING GATE

A. Experimental procedure

The qubits are first optically pumped into the state $|00\rangle$. Subsequently, they are both initialized in the superposition state $|{+}{+}\rangle$ by applying a resonant $\pi/2$-pulse to each of the qubits. Then, the phase-modulated driving field (Eq. (1)) is applied to both qubits for duration t with Rabi frequency Ω_1 set close to the COM mode frequency, ν. The difference ϵ between ν and Ω_1 is determined by the effective Lamb-Dicke parameter, η and by ν as detailed in Sec. IV C, Eq. (10). Here, we use $\Omega_1 = 2\pi \times 94.8$ kHz to fulfill this condition. Ω_2, characterizing the phase modulation depth, is set to $\Omega_2 = 2\pi \times 71$ kHz, for double dressing and protecting the qubit's coherence against RF amplitude fluctuations. For a chosen Ω_1, the value of Ω_2 is given by assumptions described in Sec. IV C and guided by numerical simulations, searching for the minimal residual excitation of the ions' motion. To reconstruct the density matrix ρ, after application of the gate, tomography

of the two- qubit state is carried out. For this purpose, the sequence of initial state preparation, subsequent two-qubit entangling gate, and measurement is repeated M times ($200 < M < 600$). After preparation of the entangled state, in order to effectively measure in different bare state bases, different sets of local single-qubit rotations are applied before a projective measurement in the $z-$basis takes place [26] (for details see appendix C).

B. Experimental results

A full reconstruction of the two qubit density matrix allows calculating the purity $\mathcal{P} = \mathrm{tr}(\rho^2)$ as well as the negativity $\mathcal{N}$ of the quantum state as basis-independent measures. Here, the purity of a state indicates the entanglement between the qubits and their state of motion. For qubit and motional states that are perfectly disentangled at the end of the gate as desired, the purity of the state is unity, while deviations from unity are attributed to residual entanglement with phonons. For a maximally entangled state (such as a Bell state $|\Phi^+\rangle = (|00\rangle + |11\rangle)/\sqrt{2}$ and $|\Psi^+\rangle = (|01\rangle + |10\rangle)/\sqrt{2}$) the negativity is 0.5. The evolution of negativity from zero (the unentangled 2-qubit state) towards the value of 0.5 (that indicates a maximally entangled state) reaching the experimental maximum of 0.48^{+2}_{-6}, is shown in Fig. 4.

The statistical error of the negativity is calculated as standard error of a set of numerically sampled density matrices. Here, we assume the entries of the reconstructed density matrix to be the mean value of a normal distribution with the width of the standard error assigned during the reconstruction (see appendix D for details). Due to this reconstruction, the error interval might exceed physical limits. In this case, we truncate the statistical error bars of physical quantities. Similarly, we truncate the error interval of fidelity and purity values which are based on Gaussian propagation of normal distributions.

An oscillation in the state's purity between ≈ 0.6 and 1.0 is evident in Fig. 4. This is due to varying qubit-phonon entanglement during the gate evolution time. This oscillation is a direct indication of the phase space trajectory generated by the gate, where at half the gate time, the purity is minimal and at the gate time, the purity is recovered (compare also Fig. 3). This indicates that one closed loop in phase space during the evolution of the gate has been completed, realizing the fastest possible two-qubit gate for the parameter set used here.

Based on the time evolution measurements of the product-state excitation probability in the bare state basis (see appendix E), we select a gate time where the product state excitation probability matches the Bell state $|\Phi^+\rangle$, *i.e.* $P_{|00\rangle} = P_{|11\rangle} = 0.5$ and $P_{|01\rangle} = P_{|10\rangle} = 0$, or the Bell state $|\Psi^+\rangle$, *i.e.* $P_{|00\rangle} = P_{|11\rangle} = 0$ and $P_{|01\rangle} = P_{|10\rangle} = 0.5$. The gate time for generating a the Bell state $|\Phi^+\rangle$ is $t_g^{\mathrm{exp}} = 313$ μs, while the Bell state $|\Psi^+\rangle$ is generated after time ($t_g^{\mathrm{exp}} = 310$ μs). Fig. 5 shows the

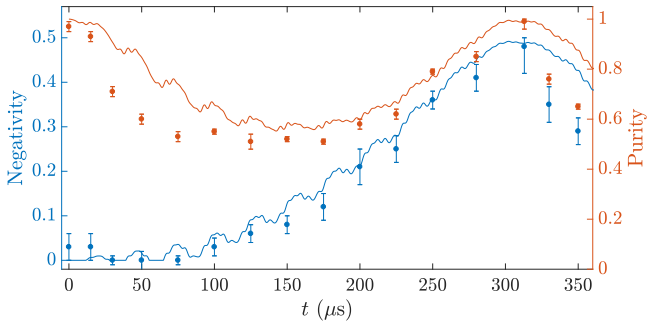

Figure 4: Time evolution of the two-qubit entangling gate quantified by the two-qubit state's negativity and purity, calculated from a full state reconstruction at interaction times t. Throughout the gate evolution, the negativity increases to 0.48^{+2}_{-6} at time $t = 313$ μs. This evolution time creates the Bell state explicitly shown in Fig. 5. The oscillation between purity of ≈ 0.6 and 1.0 indicates varying qubit-phonon entanglement during the gate evolution signifying no entanglement between qubits and motional states at the beginning and end of the gate sequence. Here the achieved pururity at the gate time $t = 313$ μs is 0.99^{+1}_{-3} . Based on Eq. (1), the gate evolution is simulated using $\Omega_1 = 2\pi \times 94.8$ kHz, $\Omega_2 = 2\pi \times 71$ kHz, and a trap frequency of $\nu = 2\pi \times 98.08$ kHz yielding the gate time $t_g^{\mathrm{sim}} = 309.5$ μs.

reconstructed density matrices, corrected for state detection errors (details are given in appendix B).

For $t_g^{\mathrm{exp}} = 313$ μs, we report measurement outcomes of $\mathcal{N} = 0.48^{+2}_{-6}$ and $\mathcal{P} = 0.99^{+1}_{-3}$. Once the density matrix is reconstructed, numerically an optimal set of single qubit rotations is computed to rotate the entangled state into a desired Bell state. While the entangling gate's parameters are chosen such that the produced state is close to $|\psi\rangle = |\Phi^+\rangle$ ($|\Psi^+\rangle$), these numerical single-qubit rotations are applied to infer the resulting state fidelity as

$$\mathcal{F} = \max_{\alpha_1,\beta_1,\gamma_1,\alpha_2,\beta_2,\gamma_2} \langle\psi|R_1^\dagger R_2^\dagger \rho R_1 R_2|\psi\rangle \qquad (4)$$

where $R_j(\alpha_j, \beta_j, \gamma_j)$ represents the rotation of qubit j around the angles α_j, β_j, and γ_j. A fidelity of $\mathcal{F} = 98^{+2}_{-3}$ % *w.r.t* a maximally entangled $|\Phi^+\rangle$ Bell state is achieved (see appendix D). For a gate time of $t_g^{\mathrm{exp}} = 310$ μs, we report $\mathcal{N} = 0.47^{+3}_{-6}$ and $\mathcal{P} = 0.98^{+2}_{-3}$, and $\mathcal{F} = 97^{+3}_{-3}$ % *w.r.t* a maximally entangled $|\Psi^+\rangle$ Bell state. Both Bell states can be selectively generated by choosing appropriate gate times.

C. Gate description

The idea to use double-dressed states for two-qubit gates was first proposed in [27]. Our gate extends that scheme using the phase modulation as an effective second drive, making it robust to amplitude fluctuations. The gate operation can be readily understood in terms of its optical counterparts [1, 28, 29]. Let us observe Eq. (3) with $\Omega_2 = 0$. The Hamiltonian is similar to the Ciarc-Zoller interaction Hamiltonian [1], where Ω_1 replaces the

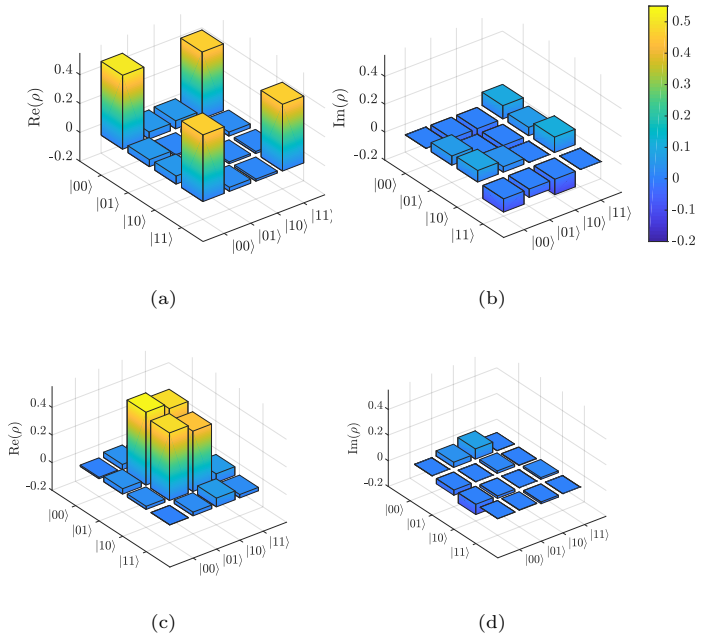

Figure 5: Reconstructed density matrices of entangled two-qubit states close to $|\Phi^+\rangle = (|00\rangle + |11\rangle)/\sqrt{2}$ (a, b) and $|\Psi^+\rangle = (|01\rangle + |10\rangle)/\sqrt{2}$ (c,d), using the phase modulated driving field for an interaction time of 310 μs and 313 μs, respectively. The resulting states close to $|\Phi^+\rangle$ and $|\Psi^+\rangle$ show a negativity of 0.48^{+2}_{-6} and 0.47^{+3}_{-6}, and a purity value of 0.99^{+1}_{-3} and 0.98^{+2}_{-3}, respectively. The reconstructed density matrices result from 200 measurements in each basis.

detuning of the laser drive frequency from the optical transition (e.g. qubit) frequency and where the carrier transition is eliminated. Therefore, in an analogous way, we can implement an entangling interaction by choosing Ω_1 to be close to the motional sidebands. The effective second drive is then used to decouple the motional mode dependent frequency shift turning the interaction into a Mølmer-Sørensen-type gate.

The entangling gate can be explained by starting from the two-qubit Hamiltonian [7],

$$H = \sum_{j=1,2} \frac{\omega_0^{(j)}}{2}\sigma_z^{(j)} + \nu b^\dagger b + \frac{\eta\nu}{2}\sigma_z^{(j)}\left(b + b^\dagger\right), \quad (5)$$

where the stretch mode is neglected as the coupling to stretch mode is smaller, and it is far detuned.

Both ions are driven with a phase-modulated drive described by the Hamiltonian given in Eq. (1), where we set $\Omega_1^{\text{Amp}} = \Omega_1^{\text{Phase}} = \Omega_1$ for both qubits. Following similar transformations as for the one qubit interaction (see appendix A), we arrive at the double dressed state Hamiltonian

$$H_{II} = \sum_{j=1,2} \frac{\Omega_2}{4}F_z^{(j)} - \frac{\eta\nu}{2}\left(F_z^{(j)}\cos(\Omega_1 t) - F_y^{(j)}\sin(\Omega_1 t)\right)\left(b\mathrm{e}^{-\mathrm{i}\nu t} + b^\dagger \mathrm{e}^{\mathrm{i}\nu t}\right). \quad (6)$$

Here, we define the double-dressed basis operators $F_z = S_x$, $F_y = S_y$, $F_z = -S_z$, and we assume the rotating wave approximation (RWA) like in the single-qubit interaction. Denoting $\Omega_1 = \nu - \epsilon$, the term proportional to $F_y^{(j)}$ in Eq. (6) is negligible, assuming that $|\epsilon \pm \frac{\Omega_2}{2}| \gg \frac{\eta\nu}{2}$, $|\Omega_1 + \nu - \frac{\Omega_2}{2}| \gg \frac{\eta\nu}{2}$, and $|\epsilon| \ll \Omega_1 + \nu$. The interaction is simplified to

$$H_{II} = \sum_{j=1,2} \frac{\Omega_2^{(j)}}{4}F_z^{(j)} - \frac{\eta\nu}{4}F_z^{(j)}\left(b\mathrm{e}^{-\mathrm{i}\epsilon t} + b^\dagger \mathrm{e}^{\mathrm{i}\epsilon t}\right) \quad (7)$$

which is a Mølmer-Sørensen-like Hamiltonian, that creates the effective interaction

$$H_{eff} = -\frac{(\eta\nu)^2}{8\epsilon}F_z^{(1)}F_z^{(2)}, \quad (8)$$

at times $\epsilon t = 2\pi n$ for non-zero integer n [28, 29]. Therefore, a maximally entangled state can be achieved by initializing the qubits in the $x-$basis (an equal superposition state) and turning on the phase modulated drive for times

$$\frac{(\eta\nu)^2}{8\epsilon}t = \frac{\pi}{4} + \frac{\pi k}{2}, \quad (9)$$

where k is an integer. The shortest gate is achieved for $k = 0, n = 1$ which results in

$$\epsilon = \eta\nu, t_g = \frac{2\pi}{\eta\nu}. \quad (10)$$

For the present axial trap frequency and static magnetic gradient, this analytical gate time of 309.8 μs matches well the experimental observed one. With the simulated gate time of 309.5 μs, corresponding to the time when phonon entanglement is minimized, we expect a unitary gate fidelity of 99.3 %. The residual infidelity is attributed to the quantum stark shift remaining in the double dressed basis, which is on the order of $(\eta\nu)^2/4\Omega_2$. Therefore, the infidelity scales as $(\pi\eta\nu/2\Omega_2)^2 \sim 0.7\%$. By parameter optimization or pulse shaping methods this can be further reduced. The remaining infidelity in the measured entangling gates is explained by the effect of phonon heating.

V. CONCLUSION

The best entangling gate reported for RF-controlled ions [15], although high in fidelity, is still an order of magnitude slower (740 μs) than its optical counterparts.

In this work, we lay the theoretical and experimental framework for implementing RF driven double dressed state entangling gates with further increasing gate speed. Using this novel gate scheme, we create the Bell states $|\Phi^+\rangle$ and $|\Psi^+\rangle$ simply by choosing the appropriate interaction time of qubits with a phase-modulated driving field. Using this novel gate, fidelities up to 98^{+2}_{-3} % with

gate time of ≤ 313 μs were achieved, using readily available experimental parameters.

The qubits are double dressed by a single phase-modulated RF field which acts as continuous dynamical decoupling driving the entangling operation, and at the same time, protects the qubits' coherence. Thus, this gate is intrinsically robust against RF field amplitude fluctuations, as well as magnetic field fluctuations that otherwise would adversely affect magnetically sensitive hyperfine-qubits.

The experiments described here were carried out in a macroscopic linear Paul-trap using a relatively small magnetic field gradient (19 T/m), secular trap frequency ($2\pi \times 98$ kHz) and Rabi frequency ($2\pi \times 95$ kHz). Cryogenic surface traps with integrated permanent magnets will allow for enhanced magnetic field gradients up to 120 T/m. This will allow for even faster gates down to gate times of 50 μs. At similar heating rates and trap frequencies ν, we expect the infidelity to decrease proportionally to the gate time. This will lead to an improvement in fidelity up to 99.6 %. Based on our simulations, we conclude that the two limiting factors of the gate fidelity are (i) the unitary infidelity which can be improved by about an order of magnitude using pulse shaping and (ii) the heating of the motional quanta during gate execution. The large ion-surface distance of $d = 130$ μm in these novel cryogenic traps is favorable, since motional heating scales as $\dot{\bar{n}} \propto d^{-3.79}$ and $\dot{\bar{n}} \propto \nu^{-2.13}$[30]. This will be advantageous for high gate fidelity.

We note that RF driven Mølmer-Sørensen-type gates with a gate time comparable to the results achieved in this work have recently been reported in [31].

ACKNOWLEDGMENTS

D.C. acknowledges the support of the Clore Scholars programme and the Clore Israel Foundation. M.N, P.H., P.B., D.N. and C.W. acknowledge the support of the EU Horizon 2020 Project No.820314 (microQC) and the German Federal Ministry of Education and Research under grant number 13N15521 (MIQRO). M.N, P.H., and D.N. thank Matthias Kleinmann for fruitful discussions.

M.N. and D.C. contributed equally to this work.

Appendix A: Double dressed state of a single Qubit

We consider a single ion trapped in a harmonic potential. The Hamiltonian that describes two hyperfine states, given that the ion is subjected to a linear magnetic field gradient, is [7]

$$H = \frac{\omega_0}{2}\sigma_z + \nu b^\dagger b + \frac{\eta\nu}{2}\sigma_z\left(b + b^\dagger\right), \tag{A1}$$

where ω_0 is the transition frequency between the two hyperfine states, ν is the motional mode frequency, η is the effective Lamb-Dicke parameter, σ_i is the Pauli matrix in the i-th direction ($i = x, y, z$) and $b/b^\dagger$ is the lowering/raising operator of the motional quanta.

We drive the ion near-resonance with a phase modulated field such that

$$H_D = \Omega_1\sigma_x \cos\left(\omega_0 t + \frac{\Omega_2}{\Omega_1}\sin\left(\Omega_1 t\right)\right), \tag{A2}$$

where Ω_1 is the Rabi frequency of the RF drive and Ω_2 is a parameter quantifying the phase modulation amplitude.

The total Hamiltonian, $H + H_D$, in the rotating frame *w.r.t.* $H_0 = \frac{\omega_0}{2}\sigma_z + \frac{\Omega_2}{2}\sigma_z\cos(\Omega_1 t)$, can be written as

$$H_I \approx \frac{\Omega_1}{2}\sigma_x - \frac{\Omega_2}{2}\sigma_z\cos(\Omega_1 t) + \nu b^\dagger b + \frac{\eta\nu}{2}\sigma_z\left(b + b^\dagger\right), \tag{A3}$$

where we made the RWA assuming $\Omega_1 \ll 2\omega_0$ and $\Omega_2 \ll \Omega_1$.

We define the dressed basis operators by the canonical transformation $S_x = \sigma_z$, $S_y = \sigma_y, S_z = -\sigma_x$. The Hamiltonian in Eq. (A3) then takes the form,

$$H_I = \frac{\Omega_1}{2}S_z + \frac{\Omega_2}{2}S_x\cos(\Omega_1 t) + \nu b^\dagger b - \frac{\eta\nu}{2}S_x\left(b + b^\dagger\right). \tag{A4}$$

As in other continuous dynamical decoupling schemes, DC noise components perpendicular to the dressed energy gap are suppressed as long as they are much smaller than Ω_1. Specifically, magnetic field noise that causes a shift of the bare energy gap $\omega_0 \to \omega_0 + \delta\omega_0$ is suppressed when $\delta\omega_0 \ll \Omega_1$. Similarly, time dependent noise is suppressed, if the power spectral density of the noise at frequency Ω_1 is small. We also note that the specific choice of phase modulation in Eq. (A2) translates into an on-resonance drive on the dressed qubit in the rotating frame (Eq. (A4)).

Moving into a second rotating frame $H_1 = \frac{\Omega_1}{2}S_z + \nu b^\dagger b$, Eq. (A4) transforms to

$$H_{II} \approx \frac{\Omega_2}{4}S_x - \frac{\eta\nu}{2}\left(S_+ e^{i\Omega_1 t} + S_- e^{-i\Omega_1 t}\right)\left(b e^{-i\nu t} + b^\dagger e^{i\nu t}\right), \tag{A5}$$

where we made the RWA assuming $\Omega_2 \ll 4\Omega_1$.

We define the double dressed states operators by the transformation $F_z = S_x$, $F_y = S_y$, $F_x = -S_z$. Consequently, the Hamiltonian in Eq. (A5) can be written as

$$\begin{aligned} H_{II} =& \frac{\Omega_2}{4}F_z \\ &- \frac{\eta\nu}{2}\left(F_z\cos(\Omega_1 t) - F_y\sin(\Omega_1 t)\right)\left(b e^{-i\nu t} + b^\dagger e^{i\nu t}\right). \end{aligned} \tag{A6}$$

The effective second drive in Eq. (A4) translates into a second dressed energy gap in the double rotating frame (Eq. (A6)). This suppresses noise sources perpendicular to the double dressed energy gap that survive in the rotating frame, Eq. (A4). Specifically, amplitude fluctuations in the drive, $\Omega_1 \to \Omega_1 + \delta\Omega_1$ will cause the dressed

energy gap to fluctuate, reducing the coherence time of the dressed qubit. These will be suppressed as long as $\Omega_2 \gg \delta\Omega_1$.

Another noise source arises from the coupling of the internal qubit states to the motional states. To unfold this statement, we first take $\Omega_2 = 0$, which describes a Rabi experiment. Then Eq. (A5) describes the undesired coupling to the motional states in the dressed basis. Assuming that $\Omega_1 + \nu \gg \eta\nu$, the interaction can be written as

$$H_{II} \approx -\frac{\eta\nu}{2}\left(S_+ b e^{-i(\nu-\Omega_1)t} + S_- b^\dagger e^{i(\nu-\Omega_1)t}\right). \quad \text{(A7)}$$

The Hamiltonian in Eq. (A7) creates an effective shift on the dressed basis that depends on the motional state of the ion. In the limit $\eta\nu \ll |\nu - \Omega_1|$ it can be described by [32]

$$H_{qss} = -\frac{(\eta\nu)^2}{2(\nu-\Omega_1)} S_z b^\dagger b. \quad \text{(A8)}$$

Therefore, if the motional state is far from the motional ground state we will observe a decay in the Rabi oscillations due to this state dependent frequency shift.

The effective second drive decouples this interaction as well when $\Omega_2 \gg \eta\nu$ and as long as $|\Omega_1 - \nu| \ll \Omega_2 \ll \Omega_1 + \nu$. In the laser-free trapped ion setting, using a static magnetic field gradient, this allows to counter further decoherence induced by the motional states.

Appendix B: Detection correction

The qubit readout is realized by collecting resonance fluorescence using a global laser beam close to 369 nm. The fluorescence of each ion is imaged onto an EMCCD camera, producing a spatially resolved image of the ion chain. Using a two-threshold method to analyze the collected fluorescence, we distinguish the qubit's logical states $|0\rangle$ and $|1\rangle$ [33]. For the experiments reported here, the product state probabilities P_i, $i = 1, 2, 3, 4$ of the computational basis states $\{1 : |00\rangle, 2 : |01\rangle, 3 : |10\rangle, 4 : |11\rangle\}$ need to be reconstructed. Due to imperfect spatial separation of the ions' fluorescence, the readout may be assigned wrongly. To account for this detection error, we carry out a correction of the detected excitation probabilities of the product states. To this end, we prepare all possible computational basis states by first optically pumping into state $|00\rangle$, then applying a Rapid Adiabatic Passage (RAP)[34] pulse, specific for the state to prepare, and finally read out the ions' internal state. In this way, the probabilities of wrong assignments of readouts can be inferred. Here, P_1, P_2, P_3 and P_4 are the excitation probabilities of state $|00\rangle$,$|01\rangle$,$|10\rangle$, and $|11\rangle$ respectively. $\widetilde{P}$ is the measured excitation probability assigned using the double threshold detection. The state vector

$$\vec{P} = (P_1, P_2, P_3, P_4), \quad \text{(B1)}$$

therefore, describes the excitation probability of all computational basis states. A linear map, M between the real probability vector $\vec{P}$ and the apparent probability $\vec{\widetilde{P}} = M\vec{P}$ can be found. Here, M is a real-valued 4×4 matrix, and the elements of M are given by the measured probabilities i.e $M_{ji} = \widetilde{P}_i$. This linear map, therefore, contains all possible wrong assignments. Applying the inverse matrix $\vec{P} = M^{-1}$ allows for reconstructing the excitation probabilities of the ions' state, compensating for detection errors: $\vec{P} = M^{-1}\vec{\widetilde{P}}$. For the two-qubit system, we show as an example the corresponding detection matrix in Fig. 6. Assuming that all statistical errors follow a normal distribution, the error of the readout correction can be propagated following the descriptions in [35]. The standard deviation of the inverse matrix's elements is

$$\sigma^2_{M^{-1}_{\alpha\beta}} = \sum_{i,j}\left(M^{-1}_{\alpha i}\sigma_{M_{ij}}M^{-1}_{j\beta}\right)^2. \quad \text{(B2)}$$

Using Gaussian error propagation, the standard errors of the reconstructed state is

$$\sigma^2_{P_i} = \sum_j\left(M^{-1}_{ij}\sigma_{\widetilde{P}_j}\right)^2 + \sum_j\left(\widetilde{P}_j\sigma_{M^{-1}_{ij}}\right)^2. \quad \text{(B3)}$$

Since the correction of readout error is not guaranteed to be unitary, using this correction for detection errors might result in nonphysical probabilities exceeding the interval $[0, 1]$. In further analysis, we therefore truncate nonphysical quantities. For the $|\Psi^+\rangle$($|\Phi^+\rangle$) Bell state, the reconstructed density matrix has one negative eigenvalue of -0.04(-0.05).

Appendix C: Tomography

The density matrix of a quantum state can be expanded into a superposition of mutually orthogonal basis operators A_i,

$$\rho = \sum_{i=1}^{15}\lambda_i A_i, \quad \text{(C1)}$$

where the coefficients λ_i are the expectation values of the operators shown in Tab. I. Following [36], we reconstruct the density matrix for a two-qubit system by measuring the expectation values $\langle\sigma_i \otimes \sigma_j\rangle, i, j = 0, 1, 2, 3$, where σ_i runs over the set of Pauli matrices $\mathbb{1}, \sigma_x, \sigma_y, \sigma_z$. In the experiment described here, only the σ_z eigenvalue can be measured directly by a projective measurement detecting resonance fluorescence near 369 nm. Therefore, in the two-qubit system investigated here, we can only directly measure the observables

$$O_1 = \sigma_z \otimes \mathbb{1} \quad \text{(C2)}$$

$$O_2 = \mathbb{1} \otimes \sigma_z \quad \text{(C3)}$$

$$O_3 = \sigma_z \otimes \sigma_z \quad \text{(C4)}$$

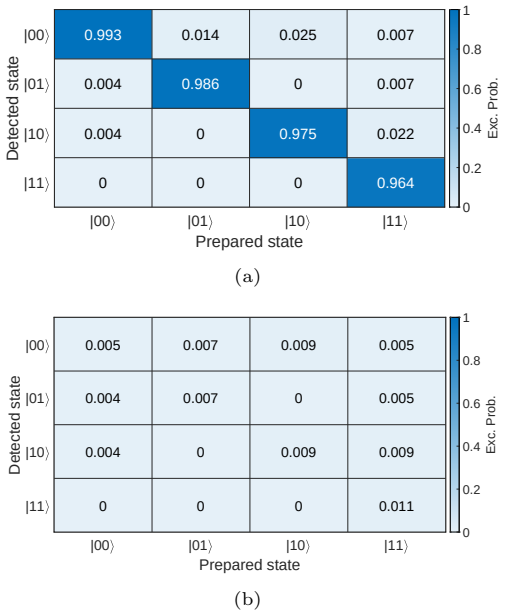

Figure 6: Determining the detection matrix M. (a) The matrix entries are conditional probabilities measured for computational basis states. (b) The standard error of the matrix in (a) is calculated according to Eq. (B3)

The corresponding expectation values are calculated using the experimental probabilities as,

$$\lambda_1^{(k)} = P_{|00\rangle} + P_{|01\rangle} - P_{|10\rangle} - P_{|11\rangle} = \langle \sigma_z \otimes \mathbb{1} \rangle \quad \text{(C5)}$$

$$\lambda_2^{(k)} = P_{|00\rangle} - P_{|01\rangle} + P_{|10\rangle} - P_{|11\rangle} = \langle \mathbb{1} \otimes \sigma_z \rangle \quad \text{(C6)}$$

$$\lambda_3^{(k)} = P_{|00\rangle} - P_{|01\rangle} - P_{|10\rangle} + P_{|11\rangle} = \langle \sigma_z \otimes \sigma_z \rangle. \quad \text{(C7)}$$

Measuring the expectation values of σ_x and $\sigma_y$is realized by mapping the quantum state onto the eigenvector of σ_z, by applying single qubit rotations $R(\theta, \phi)$. We apply nine different sets of qubit rotations, shown in Tab. I, to extract all 16 expectation values. $\lambda_i^{(k)}$, is the expectation value of the observable O_i after the qubit rotation (k), shown in the k-th row of Tab. I, is applied. The reconstructed density matrix then is given by

$$\begin{aligned}
\rho = \frac{1}{4}(&\lambda_1^{(1)} \cdot \sigma_z \otimes \mathbb{1} + \lambda_2^{(1)} \cdot \mathbb{1} \otimes \sigma_z + \lambda_3^{(1)} \cdot \sigma_z \otimes \sigma_z \\
&+ \lambda_1^{(2)} \cdot \sigma_x \otimes \mathbb{1} + \lambda_3^{(2)} \cdot \sigma_x \otimes \sigma_z \\
&+ \lambda_1^{(3)} \cdot \sigma_y \otimes \sigma_z + \lambda_3^{(3)} \cdot \sigma_y \otimes \sigma_z \\
&+ \lambda_2^{(4)} \cdot \mathbb{1} \otimes \sigma_x + \lambda_3^{(4)} \cdot \sigma_z \otimes \sigma_x \\
&+ \lambda_2^{(5)} \cdot \mathbb{1} \otimes \sigma_y + \lambda_3^{(5)} \cdot \sigma_z \otimes \sigma_y \\
&+ \lambda_3^{(6)} \cdot \sigma_x \otimes \sigma_x \\
&+ \lambda_3^{(7)} \cdot \sigma_x \otimes \sigma_y \\
&+ \lambda_3^{(8)} \cdot \sigma_y \otimes \sigma_x \\
&+ \lambda_3^{(9)} \cdot \sigma_y \otimes \sigma_y).
\end{aligned}$$

k	Ion 1	Ion 2	Exp. values		
1	-	-	$\langle \sigma_z \otimes \mathbb{1} \rangle$	$\langle \mathbb{1} \otimes \sigma_z \rangle$	$\langle \sigma_z \otimes \sigma_z \rangle$
2	$3\pi/2$	-	$\langle \sigma_x \otimes \mathbb{1} \rangle$	-	$\langle \sigma_x \otimes \sigma_z \rangle$
3	π	-	$\langle \sigma_y \otimes \mathbb{1} \rangle$	-	$\langle \sigma_y \otimes \sigma_z \rangle$
4	-	$3\pi/2$	-	$\langle \sigma_x \otimes \mathbb{1} \rangle$	$\langle \sigma_z \otimes \sigma_x \rangle$
5	-	π	-	$\langle \sigma_y \otimes \mathbb{1} \rangle$	$\langle \sigma_z \otimes \sigma_y \rangle$
6	$3\pi/2$	$3\pi/2$	-	-	$\langle \sigma_x \otimes \sigma_x \rangle$
7	$3\pi/2$	π	-	-	$\langle \sigma_x \otimes \sigma_y \rangle$
8	π	$3\pi/2$	-	-	$\langle \sigma_y \otimes \sigma_x \rangle$
9	π	π	-	-	$\langle \sigma_y \otimes \sigma_y \rangle$

Table I: The density matrix of a two-qubit system is reconstructed by mapping the quantum state to the σ_z basis. This is realized applying either one of the transformations k, which correspond to single-qubit rotations $R(\pi/2, \phi)$. Subsequently, the state is read out in the σ_z basis to reconstruct expectation values.

Assuming standard errors and using Gaussian error propagation, the variance of the real and imaginary parts of ρ are obtained.

Appendix D: Negativity

In this work, we use negativity $\mathcal{N}$ to quantify the degree of entanglement. $\mathcal{N}$ is a state-indepedent measure of entanglement, which is defined as the absolute value of the sum of the negative eigenvalues of ρ^{Γ_A} [37]. Here, ρ^{Γ_A} is the partial transpose of the two-qubit density matrix with respect to the subset of the first qubit. For a maximally entangled state, the negativity is equal to 0.5. The measure is meaningful, since a mixed two-qubit state is entangled if and only if its partial transpose has a negative eigenvalue. The statistical error of this measure is calculated by generating a set of density matrices based on a Gaussian probability distribution using the entries of the measured density matrix as mean and the statistical error as width of the distribution (see Fig. 7). Sampling the negativity of all generated density matrices, give the standard deviation of the measured density matrix.

Appendix E: Gate evolution in the computational basis

To investigate the full gate evolution in terms of the excitation probability in bare state basis, we apply a resonant $\pi/2$-pulse to both ions, bringing them into a superposition state. Then, the phase modulated driving field interacts with the ions for time t. Fig. 8 shows the two-qubit product state excitation probabilities $P_{|ij\rangle}$ (i, j denote qubit states.) The left column presents the initial stage of the time evolution, while the right column presents the time evolution around the entangling gate time. The experimental results are overlapped with simulation results agreeing well with the experimental results by using the parameters $\nu = 2\pi \times 97.85$ kHz, $\Omega_1 = 2\pi \times 94.83$ kHz, and $\Omega_2 = 23 \times \eta\nu$ for the simu-

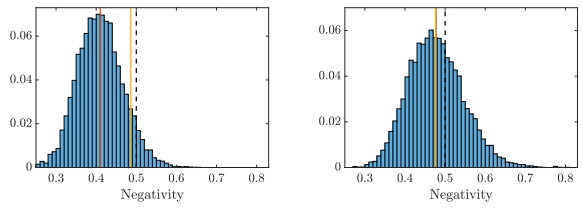

(a) (b)

Figure 7: Numerically obtained probability distribution of the negativity for the $|\Phi^+\rangle$ (a) and $|\Psi^+\rangle$ (b) Bell state. The histogram is synthesized by sampling a set of density matrices based on a Gaussian probability distribution using the entries of the measured density matrix as mean and the statistical error as width of the distribution. The orange line shows the mean of the probability distribution, and the yellow line indicates the directly calculated value of the original measured density matrix. The dashed line shows the optimal value for a pure, maximally entangled state.

lation. The dashed blue (orange) vertical line illustrates the selected gate time at which the excitation probability matches the $|\Phi^+\rangle$ ($|\Psi^+\rangle$) Bell state.

Appendix F: Gate robustness

In a double dressed frame, addressing errors occur due to detunings $\delta\Omega_1$ of the dressed states energy gap and the second driving field's frequency Ω_1. In addition, the gate scheme requires a well-calibrated Rabi frequency Ω_1^{Amp}, matching the chosen parameter $\Omega_1^{\mathrm{Phase}}$, explained in Eq. (1). Experimentally, we investigate the robustness of the double dressed entangling gate against symmetric (asymmetric) detunings δ_1 (δ_2) of Ω_1^{Amp} *w.r.t.* $\nu - \epsilon$ by measuring the entangled state negativity at a gate time of 313 μs with $\Omega_1^{\mathrm{Phase}} = 2\pi \times 94.8$ kHz. Fig. 9(a) shows the effect of a mismatch δ_1 between the physical Rabi frequency Ω_1^{Amp} for both ions and the phase modulation frequency $\Omega_1^{\mathrm{Phase}}$ ($\delta_1 = \Omega_1^{\mathrm{Phase}} - \Omega_1^{\mathrm{Amp}}$). Fig. 9(b) shows the impact of a mismatch of the physical Rabi frequencies between the two ions ($\delta_2 = \Omega_1^{\mathrm{Amp},1} - \Omega_1^{\mathrm{Amp},2}$), while $\Omega_1^{\mathrm{Amp},1} = \Omega_1^{\mathrm{Phase}}$ holds. For $\delta_1 \approx 3$ % and $\delta_2 \approx 8$ % of $\Omega_1^{\mathrm{Phase}}$, the measured negativity stays above 80 % of the optimal negativity, showing the robustness of the entangling gate against such mismatches of the RF field amplitude. Similar results were observed for direct implemented MS gates in [38], quantified in terms of fidelity. For small detunings, as typically occur in experiments, a quadratic dependence between negativity and detuning is observed, showing the stability against small detunings. The robustness of the gate, made it possible to scan a wide range of $\delta_{1,2}$, exceeding typical uncertainties during the experiments by two orders of magnitude.

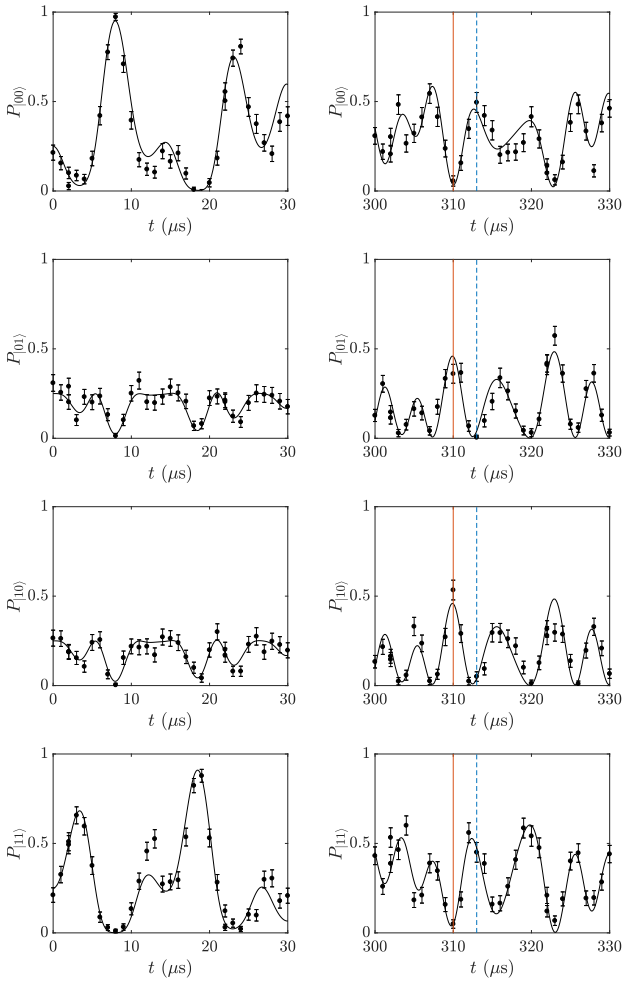

Figure 8: The gate's time evolution is measured in terms of the excitation probability in the bare state basis. The ions are initialized in the eigenstate of the dressed basis and the gate field is applied for duration t Then, the ions' states are detected. Each data point represents the result of 100 repetitions of the experiment. The orange line indicates the gate time used to implement the entangling gates for the Bell state $|\Psi^+\rangle$, and the blue dashed line marks the gate time for the Bell state $|\Phi^+\rangle$. The solid black line shows the simulated gate evolution, using parameters that best match the experimental data: $\nu = 2\pi \times 97.85$ kHz, $\Omega_1 = 2\pi \times 94.83$ kHz, and $\Omega_2 = 23 \times \eta\nu$.

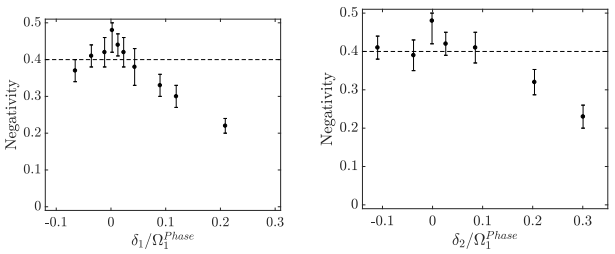

(a) (b)

Figure 9: Negativity of the two qubit state at the gate time depending on the symmetric (asymmetric) detuning δ_1 (δ_2) in the dressed state basis indicating the gate's robustness. (a) $\delta_1 = \Omega_1^{\mathrm{Phase}} - \Omega_1^{\mathrm{Amp}}$ symmetric for both ions. (b) $\delta_2 = \Omega_1^{\mathrm{Amp},1} - \Omega_1^{\mathrm{Amp},2}$while $\Omega_1^{\mathrm{Amp},1} = \Omega_1^{\mathrm{Phase}} = 2\pi\times 94.8$ kHz.

[1] J. I. Cirac and P. Zoller, Quantum computations with cold trapped ions, Phys. Rev. Lett. **74**, 4091 (1995).

[2] R. Blatt and D. Wineland, Entangled states of trapped atomic ions, Nature **453**, 1008 (2008).

[3] J. M. Pino, J. M. Dreiling, C. Figgatt, J. P. Gaebler, S. A. Moses, M. S. Allman, C. H. Baldwin, M. Foss-Feig, D. Hayes, K. Mayer, C. Ryan-Anderson, and B. Neyenhuis, Demonstration of the trapped-ion quantum ccd computer architecture, Nature **592**, 209 (2021).

[4] D. Zhu, Z. P. Cian, C. Noel, A. Risinger, D. Biswas, L. Egan, Y. Zhu, A. M. Green, C. H. Alderete, N. H. Nguyen, Q. Wang, A. Maksymov, Y. Nam, M. Cetina, N. M. Linke, M. Hafezi, and C. Monroe, Cross-platform comparison of arbitrary quantum states, Nature Communications **13**, 6620 (2022).

[5] J. P. Gaebler, T. R. Tan, Y. Lin, Y. Wan, R. Bowler, A. C. Keith, S. Glancy, K. Coakley, E. Knill, D. Leibfried, and D. J. Wineland, High-fidelity universal gate set for $^{9}Be^{+}$ ion qubits, Phys. Rev. Lett. **117**, 060505 (2016).

[6] C. J. Ballance, T. P. Harty, N. M. Linke, M. A. Sepiol, and D. M. Lucas, High-fidelity quantum logic gates using trapped-ion hyperfine qubits, Phys. Rev. Lett. **117**, 060504 (2016).

[7] F. Mintert and C. Wunderlich, Ion-trap quantum logic using long-wavelength radiation, Phys. Rev. Lett. **87**, 257904 (2001), erratum: Ion-trap Quantum Logic Using Long-Wavelength Radiation Phys. Rev. Lett. 91, 029902 (2003).

[8] C. Ospelkaus, C. E. Langer, J. M. Amini, K. R. Brown, D. Leibfried, and D. J. Wineland, Trapped-ion quantum logic gates based on oscillating magnetic fields, Phys. Rev. Lett. **101**, 090502 (2008).

[9] M. Johanning, A. Braun, N. Timoney, V. Elman, W. Neuhauser, and C. Wunderlich, Individual addressing of trapped ions and coupling of motional and spin states using RF radiation, Phys. Rev. Lett. **102**, 073004 (2009).

[10] C. Ospelkaus, U. Warring, Y. Colombe, K. R. Brown, J. M. Amini, D. Leibfried, and D. J. Wineland, Microwave quantum logic gates for trapped ions, Nature **476**, 181 (2011).

[11] A. Khromova, C. Piltz, B. Scharfenberger, T. F. Gloger, M. Johanning, A. F. Varon, and C. Wunderlich, Designer spin pseudomolecule implemented with trapped ions in a magnetic gradient, Phys. Rev. Lett. **108**, 220502 (2012).

[12] C. J. Ballance, T. P. Harty, N. M. Linke, M. A. Sepiol, and D. M. Lucas, High-fidelity quantum logic gates using trapped-ion hyperfine qubits, Phys. Rev. Lett. **117**, 060504 (2016).

[13] S. Weidt, J. Randall, S. C. Webster, K. Lake, A. E. Webb, I. Cohen, T. Navickas, B. Lekitsch, A. Retzker, and W. K. Hensinger, Trapped-ion quantum logic with global radiation fields, Phys. Rev. Lett. **117**, 220501 (2016).

[14] G. Zarantonello, H. Hahn, J. Morgner, M. Schulte, A. Bautista-Salvador, R. F. Werner, K. Hammerer, and C. Ospelkaus, Robust and resource-efficient microwave near-field entangling $^{9}be^{+}$ gate, Phys. Rev. Lett. **123**, 260503 (2019).

[15] R. Srinivas, S. C. Burd, H. M. Knaack, R. T. Sutherland, A. Kwiatkowski, S. Glancy, E. Knill, D. J. Wineland, D. Leibfried, A. C. Wilson, D. T. C. Allcock, and D. H. Slichter, High-fidelity laser-free universal control of trapped ion qubits, Nature **597**, 209 (2021).

[16] P. Barthel, P. H. Huber, J. Casanova, I. Arrazola, D. Niroomand, T. Sriarunothai, M. B. Plenio, and C. Wunderlich, Robust two-qubit gates using pulsed dynamical decoupling, New Journal of Physics **25**, 063023 (2023).

[17] C. Piltz, T. Sriarunothai, A. Varón, and C. Wunderlich, A trapped-ion-based quantum byte with 10^{-5} next-neighbour cross-talk, Nature Communications **5**, 4679 (2014).

[18] C. Piltz, T. Sriarunothai, S. S. Ivanov, S. Wölk, and C. Wunderlich, Versatile microwave-driven trapped ion spin system for quantum information processing, Science Advances **2**, e1600093 (2016).

[19] T. Sriarunothai, S. Wölk, G. S. Giri, N. Friis, V. Dunjko, H. J. Briegel, and C. Wunderlich, Speeding-up the decision making of a learning agent using an ion trap quantum processor, Quantum Science and Technology **4**, 015014 (2019).

[20] S. W. Theeraphot Sriarunothai, Gouri Shankar Giri and C. Wunderlich, Radio frequency sideband cooling and sympathetic cooling of trapped ions in a static magnetic field gradient, Journal of Modern Optics **65**, 560 (2018).

[21] I. Cohen, N. Aharon, and A. Retzker, Continuous dynamical decoupling utilizing time-dependent detuning, Fortschritte der Physik **65**, 1600071 (2017).

[22] Q.-Y. Cao, P.-C. Yang, M.-S. Gong, M. Yu, A. Retzker, M. B. Plenio, C. Müller, N. Tomek, B. Naydenov, L. McGuinness, *et al.*, Protecting quantum spin coherence of nanodiamonds in living cells, Physical Review Applied **13**, 024021 (2020).

[23] D. Farfurnik, N. Aharon, I. Cohen, Y. Hovav, A. Retzker, and N. Bar-Gill, Experimental realization of time-dependent phase-modulated continuous dynamical decoupling, Phys. Rev. A **96**, 013850 (2017).

[24] A. Salhov, Q. Cao, J. Cai, A. Retzker, F. Jelezko, and G. Genov, Protecting quantum information via destructive interference of correlated noise, arXiv preprint arXiv:2312.02267 (2023).

[25] J.-M. Cai, B. Naydenov, R. Pfeiffer, L. P. McGuinness, K. D. Jahnke, F. Jelezko, M. B. Plenio, and A. Retzker, Robust dynamical decoupling with concatenated continuous driving, New Journal of Physics **14**, 113023 (2012).

[26] C. F. Roos, G. P. T. Lancaster, M. Riebe, H. Häffner, W. Hänsel, S. Gulde, C. Becher, J. Eschner, F. Schmidt-Kaler, and R. Blatt, Bell states of atoms with ultralong lifetimes and their tomographic state analysis, Phys. Rev. Lett. **92**, 220402 (2004).

[27] I. Cohen, S. Weidt, W. K. Hensinger, and A. Retzker, Multi-qubit gate with trapped ions for microwave and laser-based implementation, New Journal of Physics **17**, 043008 (2015).

[28] A. Sørensen and K. Mølmer, Quantum computation with ions in thermal motion, Phys. Rev. Lett. **82**, 1971 (1999).

[29] K. Mølmer and A. Sørensen, Entanglement and quantum computation with ions in thermal motion, Phys. Rev. A **62**, 022311 (2000).

[30] I. A. Boldin, A. Kraft, and C. Wunderlich, Measuring Anomalous Heating in a Planar Ion Trap with Variable Ion-Surface Separation, Phys. Rev. Lett. **120**, 023201 (2018).

[31] M. A. Weber, M. F. Gely, R. K. Hanley, T. P. Harty, A. D. Leu, C. M. Löschnauer, D. P. Nadlinger, and D. M. Lucas, Robust and fast microwave-driven quantum logic for trapped-ion qubits, arXiv 10.48550/arXiv.2402.12955 (2024).

[32] D. F. James and J. Jerke, Effective hamiltonian theory and its applications in quantum information, Canadian Journal of Physics **85**, 625 (2007).

[33] N. V. Vitanov, T. F. Gloger, P. Kaufmann, D. Kaufmann, T. Collath, M. Tanveer Baig, M. Johanning, and C. Wunderlich, Fault-tolerant Hahn-Ramsey interferometry with pulse sequences of alternating detuning, Phys. Rev. A **91**, 033406 (2015).

[34] C. Wunderlich, T. Hannemann, T. Körber, H. Häffner, C. Roos, W. Hänsel, R. Blatt, and F. Schmidt-Kaler, Robust state preparation of a single trapped ion by adiabatic passage, Journal of Modern Optics **54**, 1541 (2007).

[35] M. Lefebvre, R. Keeler, R. Sobie, and J. White, Propagation of errors for matrix inversion, Nuclear Instruments and Methods in Physics Research Section A: Accelerators, Spectrometers, Detectors and Associated Equipment **451**, 520 (2000).

[36] C. Roos, G. Lancaster, M. Riebe, H. Haffner, W. Hansel, S. Gulde, C. Becher, J. Eschner, F. Schmidt-Kaler, and R. Blatt, Bell states of atoms with ultralong lifetimes and their tomographic state analysis, Phys. Rev. Lett **92**, 220402 (2004).

[37] G. Vidal and R. F. Werner, Computable measure of entanglement, Phys. Rev. A **65**, 032314 (2002).

[38] A. E. Webb, S. C. Webster, S. Collingbourne, D. Bretaud, A. M. Lawrence, S. Weidt, F. Mintert, and W. K. Hensinger, Resilient entangling gates for trapped ions, Phys. Rev. Lett. **121**, 180501 (2018).